

Vehicle Side-Slip Angle Estimation Under Snowy Conditions Using Machine Learning

Georg Novotny^{a,b} Yuzhou Liu^a Walter Morales-Alvarez^b Wilfried Wöber^{b,c}
Cristina Olaverri-Monreal^a

^a *ITS-Chair for Sustainable Transport Logistics 4.0, Johannes Kepler University, Upper Austria, Austria*
E-mails: georg.novotny@jku.at, yuzhou.liu@jku.at, walter.morales_alvarez@jku.at,
cristina.olaverri-monreal@jku.at

^b *Industrial Engineering, UAS Technikum Wien, Vienna, Vienna*
E-mails: georg.novotny@technikum-wien.at, wilfried.woeber@technikum-wien.at

^c *Institute for Integrative Nature Conservation Research, University of Natural Resources and Life Sciences, Vienna, Vienna*
E-mail: wilfried.woeber@boku.ac.at

Abstract. Adverse weather conditions, such as snow-covered roads, represent a challenge for autonomous vehicle research. This is particularly challenging as it might cause misalignment between the longitudinal axis of the vehicle and the actual direction of travel. In this paper, we extend previous work in the field of autonomous vehicles on snow-covered roads and present a novel approach for side-slip angle estimation that combines perception with a hybrid artificial neural network pushing the prediction horizon beyond existing approaches. We exploited the feature extraction capabilities of convolutional neural networks and the dynamic time series relationship learning capabilities of gated recurrent units and combined them with a motion model to estimate the side-slip angle. Subsequently, we evaluated the model using the 3DCoAutoSim simulation platform, where we designed a suitable simulation environment with snowfall, friction, and car tracks in snow. The results revealed that our approach outperforms the baseline model for prediction horizons ≥ 2 seconds. This extended prediction horizon has practical implications, by providing drivers and autonomous systems with more time to make informed decisions, thereby enhancing road safety.

Keywords: Vehicle Side-Slip Angle, Neural Network, Motion Model, Snow

1. Introduction

Novel safety systems which control vehicle dynamics monitor key sensor signals such as wheel angular velocities, steering angle, yaw rate, and vehicle side-slip angle [1]. The side-slip angle, also known as drift or attitude, represents the misalignment between the vehicle's longitudinal axis and its travel direction, making it crucial for systems like electronic stability control (ESC) to ensure safety. Vehicle control systems including the ESC, active steering, and advanced traction control (ATC) rely on real-time vehicle state assessments, particularly the vehicle side-slip angle (VSA) [2, 3]. The vehicle's state comprises longitudinal and lateral velocity or acceleration, steer-

ing angle, yaw rate, and more. These properties can be measured directly (like acceleration, steering angle) or inferred from sensor data. However, calculating the VSA is complex as it depends on wheel and ground friction, wheel forces, and vehicle dynamics [2–4]. Determining these factors directly is costly and complicated, requiring high-precision sensors [2–7]. Therefore, researchers have long investigated VSA estimation methods, starting as early as 1990 [2]. This study primarily employs an empirical descriptive model to explore and confirm the relationships between vehicle and road factors and VSA. To ensure a comprehensive understanding of these relationships, we have employed statistical analyses using both Spearman and Pearson correlation methods, allowing us to analyze

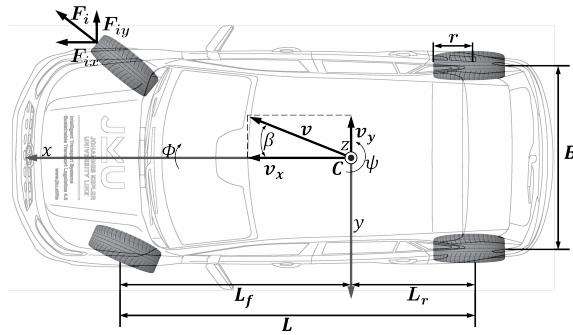


Fig. 1. Top view of a vehicle during a right turn, with a fixed coordinate frame at \mathbf{C} the center of mass. The significant physical variables encompass the longitudinal and lateral velocity v_x and v_y , wheel speeds ($\omega_{rl}, \omega_{rr}, \omega_{fl}, \omega_{fr}$), longitudinal acceleration a_x , steering angle δ and yaw and roll rate $\dot{\Psi}$ respectively $\dot{\Phi}$.

the data in multiple dimensions. As indicated in [5], the vehicle maneuverability strongly depends on the size of the VSA. Under dry road conditions the vehicle can achieve a VSA of up to ten degrees. However, in snowy conditions, this value is limited to a maximum of four degrees to ensure the vehicle remains maneuverable.

Typically, when estimating the VSA, the physical properties depicted in Fig. 1 are taken into account. These properties are either provided by (CAN) BUS data or acquired through proprioceptive sensors. In the following, we aim to provide a wide baseline for understanding the performance of various VSA estimate methodologies, particularly under diverse situations, and according to [2, 3, 8, 9], these approaches can be primarily classified as:

- Observer - based: These approaches rely either on a kinematic or dynamic model of the vehicle in combination with an observer, where the most common ones are derivatives of the bayes filter, such as kalman filter (KF) and its non-linear derivatives extended kalman filter (EKF) and unscented kalman filter (UKF).
- Neural Network - based: Most approaches rely on the same neural network (NN) structure consisting of a total of three layers composed of one input layer, one fully connected hidden layer with log-sigmoid activation, and one output layer with linear activation.

The issue of estimating the VSA becomes particularly relevant under non-optimal weather conditions such as cases involving snow-covered roadways, as described in [10]. As observer-based estimators drasti-

cally rely on models of not only the vehicle but also of the tire-road interaction, the performance of these varies according to the accuracy of the model as well as the sensor systems utilized. Moreover, the non-linear characteristics of driving make it difficult to obtain a satisfactory model and estimation performance.

The findings presented in [3] elucidate several points on vehicle dynamics. Dynamic-based observer methods apply effectively only at $\leq 50\text{km/h}$ and can falter during severe steering maneuvers. Conversely, kinematic-based observers offer accurate results under high lateral accelerations and can estimate VSA at high velocities. However, their error accumulation renders them ineffective over extended periods. Finally, NN based methods emerged as the top performers in their tests.

In [4] four different NN estimators for VSA estimation were compared: feed forward neural networks (FFNN) [11], recurrent neural networks (RNN) [12], gated recurrent units (GRU) [13], and long short-term memory (LSTM) [14]. These networks were compared in terms of accuracy based on the root mean square error (RMSE), mean training time, and mean estimation time. They concluded that FFNN achieved the highest accuracy and lowest estimation time but also the highest training time. LSTM outperformed GRU in terms of accuracy, but took longer for each prediction and overall training.

As stated at the beginning of this section, accurate estimation of the VSA is crucial for efficient ESC, which in turn can significantly mitigate vehicle spinning - a primary contributor to nearly 25% of human-injury-related accidents [4].

Prompted by this necessity, we contribute to the state of the art in VSA estimation, by proposing an enhanced sensor configuration and a novel approach to integrate sensor data for more precise estimation over an extended prediction horizon.

We present a model for estimating VSA on snowy roads - a challenging scenario for ESC systems [5]. **Building on the premise that exteroceptive sensor data, strictly speaking visual characteristics, can enhance prediction accuracy [15, 16], we introduce an approach that integrates image features extracted by a convolutional neural network (CNN) [17] into a hybrid artificial neural network [8].** This method leverages the rich visual cues from CNN-processed camera feeds, thereby uncovering previously unexplored VSA-related information and improving prediction accuracy over existing techniques.

Camera-based features provide extensive information about road conditions, including wet, icy, or uneven surfaces thus enabling the system to adapt to diverse road scenarios. Additionally, they capture visual cues related to vehicle dynamics, such as relative orientation or position changes during adverse conditions like snow, which enhance the understanding of the vehicle's state. Furthermore, this integration reduces the model's reliance on potentially erroneous sensors and enhances the overall reliability of VSA estimation.

Our model surpasses current research [3, 4, 8] in terms of an extended prediction horizon and combines the benefits of FFNN and GRU-based VSA estimation methods with deep learning-driven perception models. We also incorporate a kinematic model as outlined in [8] to strengthen the prediction capabilities of our convolutional neural network gated recurrent unit (CNN-GRU) architecture.

The verification of our approach was conducted at two levels:

1. We scrutinized the correlation between the image features and the VSA by employing Pearson's correlation coefficient and Spearman's rank correlation coefficient [18]. This evaluation utilized a simulated dataset, where both CNN features [17] and side-slip angles were collated. The collected image features underwent preprocessing through principal component analysis (PCA) [19]. The resulting relationship between the reduced image features and the side-slip angle was then further examined and analyzed.
2. To evaluate the proposed model, we integrated the extracted image features into a pipeline based on a GRU. The model's performance was evaluated by comparing its results with the ground truth (GT) values from a separate evaluation dataset and a baseline model, as described in [8].

This article is structured as follows: The following Section 2 introduces the problem of VSA and the general architecture for NN-based estimation approaches, further we provide preliminary information on the utilized NN architectures (CNN, GRU) as well as on the motion model (single-track model) utilized in this research. In Section 3 related literature on research estimating the VSA as well as approaches combining CNNs with GRU networks are reviewed, followed by our proposed approach in Section 4. The results are presented and discussed in Sections 5 and Section 6 respectively. Finally, Section 7, concludes the manuscript and presents future work.

2. Foundational Concepts and Approaches

This section lays the foundation for understanding the complexities of vehicle dynamics and the perception models used for their prediction, focusing primarily on the vehicle side-slip angle estimation problem. The challenges of accurately determining the side-slip angle with conventional methods lead to the exploration of machine learning-based alternatives. Through exploring neural networks and kinematic constructs, this section offers a concise overview of the methodologies implemented in this work.

For a technical explanation of the CNN, GRU architecture or the single-track model the authors refer the reader to [13, 20–23].

2.1. Vehicle Side-Slip Angle Estimation Problem

Centered on a vehicle's mass, its motion is characterized in a horizontal celestial system. The overall velocity ${}^C v$, at the vehicle's center of mass, is a composite of longitudinal v_x and lateral v_y velocities. The angular velocity around the yaw direction z -axis is defined as yaw-rate $\dot{\Psi}$, while $\dot{\Phi}$ and $\dot{\Theta}$ depict rotational speeds in roll and pitch directions. **Side-slip angle β** , a pivotal metric in vehicle dynamics, describes the deviation between the vehicle's longitudinal axis and its actual direction of movement, specifically representing the angle between v and the vehicle's orientation. If the vehicle drifts along the velocity vector at a 90-degree angle, β indicates a perpendicular turn of the vehicle's longitudinal axis to the left.

β can be calculated using trigonometry if we could determine the center of mass and the vector components (v_x , v_y) of the total velocity ${}^C v$ at the vehicle's center of mass accurately, as shown in Eq. 2.1.

$$\beta = \arctan \left(\frac{v_y}{v_x} \right) \quad (2.1)$$

with

$${}^C v = \begin{bmatrix} v_x \\ v_y \\ 0 \end{bmatrix} = \begin{bmatrix} v \cdot \cos\beta \\ v \cdot \sin\beta \\ 0 \end{bmatrix}$$

However, accurate determinations are impractical, which necessitates the exploration of alternative VSA estimation methods. Typically, VSA ranges from

-4 to 4 degrees during regular driving [8]. Dynamic factors such as tire forces, roll angle, and kinematic aspects like vehicle mass or structure significantly influence VSA estimation. Observer-based methods often utilize these values, but their limitations are apparent due to issues with measurement accuracy and road-surface condition detection. Machine learning offers promising solutions for these challenges and relevant literature will be discussed in the next section.

2.2. Machine Learning Essentials: CNNs and GRUs

Machine learning models, particularly CNNs and GRUs, have become increasingly popular in the realm of artificial intelligence in recent years. While CNNs have proven their proficiency in tasks such as human action recognition, object detection, and natural language processing, GRUs have found applications in time series forecasting [24], semantic analysis [25], and also natural language processing [26]. In the realm of VSA estimation, machine learning models, especially CNNs and GRUs, offer significant advantages in contrast to traditional approaches. CNNs aim to extract spatial features from images which makes them suitable for processing visual data from cameras to detect road conditions and vehicle dynamics. On the other hand, GRUs are adept at handling sequential data capturing the temporal dependencies in VSA estimations over time.

2.2.1. Convolutional Neural Networks

CNNs, a variant of deep feed-forward artificial neural network (ANN)s, are effective in applications such as image analysis [27], and natural language processing [28] due to their high-dimensional vector handling capability.

CNNs consist of feature extraction and classification parts, where alternating convolutional and pooling layers create feature maps. Information propagates from early layers, holding low-level details, to later layers with high-level details. The reduced-dimensionality output from the last feature extraction layer is input to a fully connected layer for classification.

CNNs' core components are (i) convolutional layers, (ii) pooling layers, and (iii) fully-connected layers.

Convolutional Layer: These layers utilize kernels to perform convolution operations on input data, traditionally utilized for tasks such as blurring and information extraction, but primarily aimed at extracting features from spatial data in this context. By utilizing weighted kernels, these layers generate feature maps

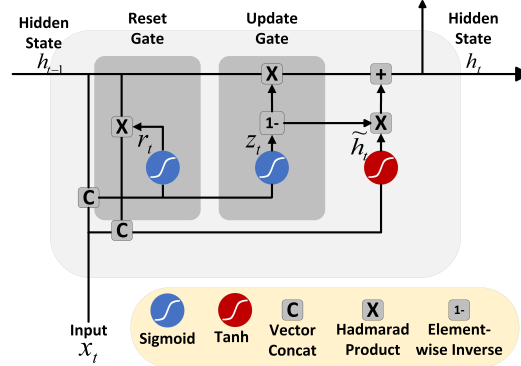


Fig. 2. Single GRU cell architecture. This showcases the primary components including the input layer that receives data, the hidden state carrying information through the network, the reset gate which determines the extent to which previous information is forgotten, and the update gate that decides how much of the current state should be updated with the new proposed state.

from input images. The process involves applying activation functions like the ReLU activation function to neurons and conducting convolution at each point between the kernel and image. This operation of convolution helps detect features like edges, consequently enhancing image sharpness for specific tasks.

Pooling Layer: This layer aggregates input data to create downsampled outputs by utilizing a summary statistic, enhancing efficiency, reducing overfitting, and retaining spatial invariance, but with lower spatial dimensions. The pooling operation can be seen as a form of image averaging (blurring) that retains the most salient features while reducing dimensionality.

Fully-Connected Layer: In this layer all inputs from the preceding layer link to every activation unit of the next layer, creating a high-level feature map. This layer integrates the extracted features, supporting tasks like object recognition or classification based on the detected patterns.

2.2.2. Gated Recurrent Unit

GRUs, introduced in [13], are a type of RNN [12] designed to capture long-term dependencies in sequential data while overcoming the short-term memory limitations of traditional RNNs. They have comparable accuracy to other RNN structures like LSTM [14], but offer faster training and prediction due to fewer model parameters [29, 30].

As Fig. 2 illustrates, the GRU cell is governed by:

$$r_t = \text{sigm} (W_{xr}x_t + W_{hr}h_{t-1} + b_r) \quad (2.2)$$

$$z_t = \text{sigm} (W_{xz}x_t + W_{hz}h_{t-1} + b_z) \quad (2.3)$$

$$\tilde{h}_t = \tanh(W_{xh}x_t + W_{hh}(r_t \odot h_{t-1}) + b_h) \quad (2.4)$$

$$h_t = z_t \odot h_{t-1} + (1 - z_t) \odot \tilde{h}_t \quad (2.5)$$

where x_t , r_t , z_t , \tilde{h}_t , h_t are the input vector, reset gate, update gate, candidate hidden state vector, *sigm* is the sigmoid function, and output vector at time t , respectively.

Reset Gate: The reset gate (r_t) determines what information to keep from the past and present input, providing a "short-term memory". It outputs a binary value for each input, indicating whether to discard (0) or keep (1) information from the previous time step.

Update Gate: The update gate (z_t) decides how much of the past hidden state (h_{t-1}) to retain for the future, and serves as a "long-term memory". Like the reset gate, the update gate outputs a binary value for each input, thus provides selective information retention.

It's worth noting that while GRUs inherently transfer information across time steps in a sequence, this mechanism is distinct from the traditional concept of transfer learning, where pre-trained models are adapted for a different but related task [30, 31]

2.3. Single Track Model

The single-track model, a physics-based kinematic model often used as a simplified version of the Ackermann steering model [23, 32], delivers a plausible representation of vehicle behavior without requiring extensive modeling or parameterization [22, 32]. This kinematic model was proposed for lateral accelerations below 0.5g [32].

The bicycle model, a simplified version of the Ackermann model, as depicted in Fig. 3a, merges the front and rear wheels into single points each. This enables the model to depict lateral vehicle dynamics in a physically plausible manner as illustrated in Fig. 3b [22, 33]. The single-track model's acceleration around the center of gravity is given by:

$$\vec{a} = \begin{bmatrix} a_x \\ a_y \\ a_z \end{bmatrix} = \begin{bmatrix} -v(\dot{\psi} + \dot{\beta}) \sin \beta \\ v(\dot{\psi} + \dot{\beta}) \cos \beta \\ 0 \end{bmatrix} \quad (2.6)$$

In the single-track model, the vehicle's mass is assumed to be concentrated at its center of gravity, a common simplification in vehicle dynamics. While this assumption streamlines the model, it may overlook

some real-world complexities. However, neural networks, especially CNNs and GRUs, can learn and account for such intricacies. Leveraging the deep learning capabilities highlighted by [34], our hybrid CNN-GRU architecture learns transformations, including those related to the center of mass, enhancing the model's adaptability and accuracy.

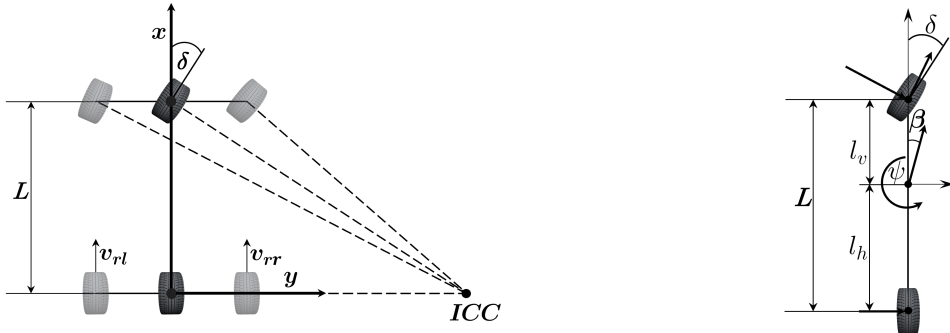
3. State of the Art

In this section, we address the topic of VSA estimation as well as CNN-GRU hybrid models. As outlined in the introduction, the majority of VSA estimation methods gravitate towards either a model-based approach, employing a kinematic or dynamic model coupled with an observer, or a black-box model which utilize machine learning models. However, only a few of these approaches exploit a combination of both strategies.

In [35], three FFNN configurations were designed to estimate the VSA. Network A utilized basic vehicle dynamics, while Networks B and C integrated time-delayed signals and feedback for improved accuracy. While A faced challenges with speed variations, B showed adaptability, and C, despite its feedback mechanism, had inconsistent performance. Overall, Network B was the most reliable for estimating the sideslip angle across varying conditions.

The authors of [9] utilized an LSTM RNN in combination with a fully connected layer as output to determine the lateral vehicle velocity which is inherently necessary to calculate the VSA. They collected approx. 88 minutes of simulation data with varying road friction coefficients and applied a 90/10 train-test split. For evaluation they performed a double lane change experiment and reported that their method achieved accurate estimation of the vehicle lateral velocity during low and medium speeds of ≤ 50 km/h regardless of the road friction. However, they stated that their model did not fully learn the vehicle dynamics as it performed poorly at the tested speed of 70 km/h.

In [8] a GRU network was combined with a kinematic model for the estimation of the VSA. The authors collected approx. 16 hours of sensor data, in a real-world vehicle, under three different road conditions and compared their VSA estimation approach with a sensor fusion of global positioning system (GPS) and inertial measurement unit (IMU). The authors set a plain GRU network against a hybrid kinematic GRU model for comparison. The former model



(a) Simplified bicycle model based on Ackermann steering model. The image illustrates the rudimentary geometric interpretation of vehicle turning based on the instantaneous center of curvature (ICC), where the vehicle is reduced to a two-wheel model with the front wheel performing the steering. Adapted from [5, 22, 23]

(b) Single-Track model. A simplified model used for analyzing the dynamics of a vehicle. It assumes that the vehicle's mass is concentrated in a single point and the forces and moments are evaluated in the vertical plane of symmetry. Adapted from [5, 22]

Fig. 3. Comparison between the Ackermann Steering Model and Single-Track Model

incorporated inputs such as the steering wheel angle, longitudinal speed, longitudinal and lateral acceleration, yaw rate, and all four wheel speeds for prediction. In contrast, the latter model, aside from using the previously mentioned inputs, also took into account the change in side-slip angle $\dot{\beta}$, computed by the single-track model. Their results showed that the kinematic GRU model outperformed the single GRU model and provided a mean square error (MSE) of 0.107 on dry asphalt and 0.519 on wet asphalt. On snow, the model provided the worst results with a MSE of 4.529.

The authors of [36] proposed a hybrid state estimation approach to estimate the roll angle of a vehicle using a combination of data-based estimators represented by a GRU network and existing physical knowledge. The proposed method was evaluated using real-world driving data and showed improved precision compared to traditional methods such as EKF and UKF. The results showed that the hybrid state estimation approach provided accurate estimates of roll angle compared to traditional methods such as EKF and UKF. The RMSE of roll angle estimation using hybrid state estimation was 0.23° , while EKF had an RMSE of 0.32° and UKF had an RMSE of 0.28° .

Utilizing the feature extraction capabilities of CNNs and using them as (additional) input for GRU networks has seen an up-rise in recent years as many researches combined the benefits of those two methods creating a CNN-GRU deep learning framework [37–41].

The combination of CNN and GRU was employed in [40] to learn the dynamic time-series relationship

between variable working conditions and clamping point force for the prediction of the clamp force for handling deformable parts. Here a fully connected CNN was utilized for feature extraction and dimensionality reduction of high dimensional data representing the change of force state at the clamping point. The extracted features were utilized as inputs for a GRU network for prediction of the clamping point force under complex time-varying conditions and proved the effectiveness of the CNN-GRU prediction framework.

The research conducted in [37] proposed a two-step hybrid CNN-GRU network to predict short-term electricity consumption in residential buildings. The CNN consisted of two convolutional layers with ReLU activation function and a kernel size of two and a filter of 1×16 for the first layer, respectively, 1×8 for the second layer. The extracted spatial features were then fed into a two layer GRU with a dense output layer to predict the future energy consumption. The proposed model was compared against a number of different machine and deep learning models on the IHEPC dataset and against other state of the art techniques on the AEP dataset and proved to work well.

A spatial-temporal feature-selection algorithm was also utilized in [41] to determine relevant inputs for a CNN-GRU for short-term traffic speed prediction. The network structure consisted of the LeNet-5, for the CNN, and a bidirectional GRU, so that the predictions could also incorporate previous inputs in addition to the current input vector for greater accuracy. The findings showed that this hybrid model overcame the

constraints of single models, fully utilized the space-time properties of the traffic data, and predicted traffic speeds with high accuracy.

Existing research highlights the potential of hybrid GRU models for VSA estimation, but their performance is limited in challenging conditions like snowy environments [8]. The effectiveness of hybrid CNN and GRU models for VSA estimation in adverse conditions remains largely unexplored. Our study addresses this research gap and aims to enhance VSA estimation models by integrating visual cues from camera data thus reducing reliance on error-prone sensors, particularly in challenging snowy road conditions.

To provide a clearer perspective on how our approach stands in comparison to existing literature, we present table 1 that juxtaposes the key components and features of various state-of-the-art methods with our proposed methodology. This table elucidates the comprehensive nature of our approach, highlighting its distinctiveness and advancements in the field. By examining the table, it becomes evident that our approach amalgamates a diverse set of features and methodologies, setting it apart from the current state-of-the-art literature. This comprehensive integration is pivotal in enhancing the accuracy and robustness of VSA estimation, especially under challenging conditions.

4. Simulation Environment and Data Analysis Methods

This section initially presents the simulation environment, which was used to generate the data for this

Table 1

Component comparison of state-of-the-art literature with our approach

	[8]	[9]	[35]	[36]	[37]	[40]	[41]	Our
FFNN	x	x	✓	x	x	x	x	✓
LSTM	x	✓	x	x	x	x	x	x
GRU	✓	x	x	✓	✓	✓	✓	✓
VSA Estimation	✓	✓	✓	x	x	x	x	✓
Kinematic Model	✓	x	x	x	x	x	x	✓
Snowy Conditions	✓	x	x	x	x	x	x	✓
Image Features	x	x	x	x	x	✓	x	✓
CNN-GRU Hybrid	x	x	x	x	✓	✓	✓	✓

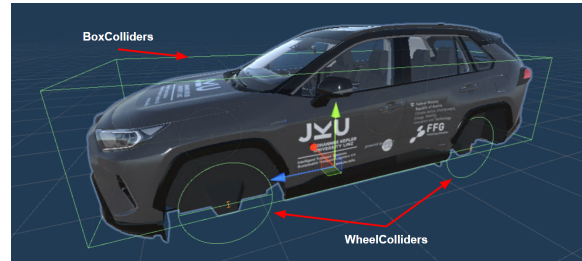


Fig. 4. The car model, as well as the BoxCollider and WheelColliders. The mesh of the wheels are disabled to avoid visual occlusion of the WheelColliders.

study. Subsequently, we outline the methodology used to explore the relationship between the image-based features and the VSA. Furthermore, this section introduces the proposed model that integrates CNN-based features for accurate VSA estimation.

4.1. Experimental Setup and Simulation Environment

We used the Unity3D based 3DCoAutoSim [42] platform to simulate the environment with snowfall, friction, and car tracks on the snow. The test ground setup used in this work is based on [10], which is a snow covered 4-lane dual carriageway circular test track. The friction between the road surface and the wheels is directly achieved by setting the Unity WheelColliders, which will be explained in more detail later. The setting of the test ground is mainly to extract visual data such as car tracks on the snow. For the dataset creation we performed multiple laps, in both directions of the course, and stored the sensor data in separate rosbag files.

The vehicle model in the simulator corresponded to a Toyota Rav4 Hybrid (2020) [43] and closely resembles it in terms of track-width, wheelbase, and mass which is equally distributed over the volume of the vehicle. In order to perform the collision volume of the vehicle, we used a Unity BoxCollider that covered the complete body of the vehicle, with its center of mass selected from the geometric center of the vehicle chassis, as seen in Fig. 4. The four wheels were respectively controlled by four Unity WheelColliders, and their steering occurred in conformity with the Ackermann steering model. The control scripts set of the vehicle relied on [10], which was implemented via the RealisticCarControl V3 [44].

The parameters of the WheelCollider controlled the friction between the wheels and ground. The default settings of the friction parameters for the experiment are shown in Table 2. We also implemented a 9 degree

of freedom Inertial Measurement Unit (IMU), GPS sensor, as well as longitudinal velocity. In addition, we monitored the steering angle of the vehicle as well as the side-slip angle. All these data were either directly received from Unity or calculated from the sensor data. Finally, we used two cameras with a resolution of 640×480 pixels as the front and rear cameras of the vehicle. The vertical field of view of the camera was 60° , the horizontal field of view depended on the aspect ratio.

4.2. Analysis of the Image Data

The foundation of this study is built upon an existing relationship between the data obtained from imaging sensors and the VSA. This approach is motivated by the acknowledged limitations of black-box machine learning models [45].

To develop a reliable model, we performed a comprehensive analysis of this relationship. This involved the collection and processing of image and VSA data from the simulated environment discussed above, conducting rigorous statistical tests to investigate correlations, and scrutinizing the relationship between the variables.

In each timestep t , we obtained $\beta_t \in \mathbb{R}$, the image $\mathcal{I}_{front,t} \in \mathbb{R}^{R \times C \times 3}$ from the front camera as well as $\mathcal{I}_{rear,t} \in \mathbb{R}^{R \times C \times 3}$ from the rear camera, where C is the number of columns of the image and R is the rows of the image.

In each timestep, we applied the GoogLeNet CNN [17] and obtained 1024 features for each image. In order to evaluate the relationship between these features and the VSA, we first standardized the features and extracted a de-correlated representation relying on the PCA [19]. We chose a variance-based method (PCA) since it offers a clear and intuitive understanding of the data's structure. The principal components (lateral dimensions) derived from such methods are orthogonal, ensuring no redundancy, and they capture the directions of maximum variance in the data, making it more readable.

Table 2

The friction parameter settings of the WheelColliders

	Forward Friction	Sideways Friction
Extremum Slip	0.4	0.2
Extremum Value	1	1
Asymptote Slip	0.8	0.8
Asymptote Value	0.5	0.75
Stiffness	1	1

The relationship between the first five principal components and the VSA was assessed using both Pearson's and Spearman's rank correlation tests. Pearson's test was chosen as it effectively measures linear relationships between continuous variables providing insights into any linear correlation between the latent features and β . On the other hand, the Spearman's rank correlation captures non-linear, monotonic relationships that might not be evident in a linear analysis. Together, these tests offer a comprehensive evaluation of both linear and rank-order correlations. The focus was primarily on the first five principal components of the CNN latent features. These components were chosen due to their significant contribution to the overall variance, thereby enhancing the effectiveness of the analysis.

We formulated two null hypotheses for our analysis.

- Null Hypothesis 1, denoted as $H_{0,Pearson}$, assumed that the correlation obtained using Pearson's correlation coefficient was zero $H_{0,Pearson} : \rho_{Pearson} = 0$.
- Null Hypothesis 2, denoted as $H_{0,Spearman}$, assumed that the correlation obtained using Spearman's correlation coefficient was zero $H_{0,Spearman} : \rho_{Spearman} = 0$.

Both hypotheses tested whether there was a significant relationship between the variables under consideration. If the p-value, the probability of observing the data or more extreme results under the assumption that the null hypothesis is true, was found to be less than the predefined significance level α of 0.001, then the null hypotheses will be rejected. We deliberately selected 0.001 as our significance level to impose a stringent criterion.

4.3. Model Implementation for VSA Estimation

Our implemented prediction model consisted of a CNN, specifically GoogLeNet [17], for feature extraction on images, and a GRU, for time series prediction, as visualized in Fig. 5. The choice of GoogLeNet was motivated by its efficiency in feature extraction, computational affordability, and its ability to learn multi-scale features through inception modules [17], metrics that are crucial in various applications, including digital photogrammetry of piping systems [46]. These evaluation criteria align with the comprehensive computational exploration conducted by [47], who also emphasized the importance of methodological choices and feature extraction techniques. The chosen inputs

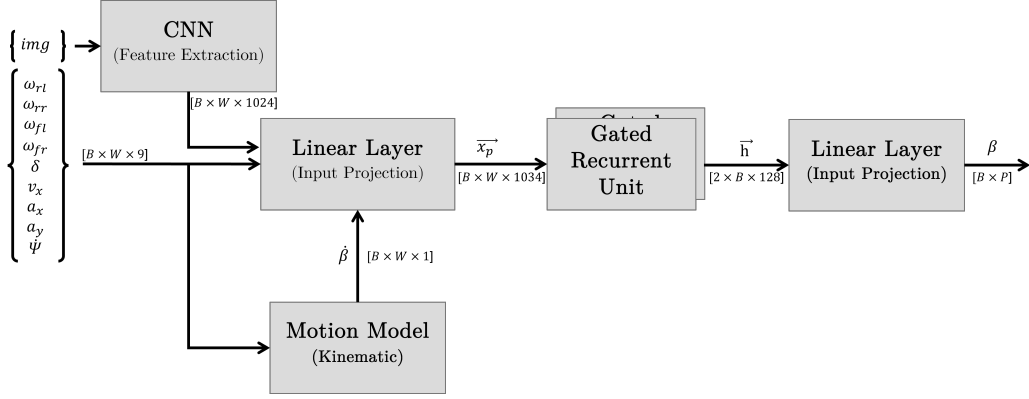


Fig. 5. The proposed method with a batch size of B , sliding window length of W and a output prediction horizon of P considering only one camera. The proposed approach utilizes various sensor data, including images (img), wheel angular velocities (ω_{xy}), steering angle (δ), longitudinal velocity (v_x), longitudinal and lateral acceleration (a_x and a_y), yaw rate ($\dot{\psi}$), as well as the derivative of the prediction target ($\dot{\beta}$) computed using the kinematic single-track model, as input for time series prediction. The model integrates a CNN [17] for image-based feature extraction and a GRU with two recurrent layers, a hidden dimensionality of 128, and a $tanh$ activation function for capturing temporal dependencies and ensuring effective information transfer across time steps. This amalgamation results in a hybrid kinematic CNN-GRU informed model that leverages exteroceptive data. The dimensionality of the various inputs, as well as the propagated values are displayed within the square brackets [].

consisted of a sliding window sequence W of a variety of sensor data typically provided via controller area network (CAN) BUS in a car (e.g. images (img), wheel velocities (ω_{xy}), steering angle (δ), longitudinal velocity (v_x), longitudinal and lateral acceleration (a_x and a_y), yaw rate ($\dot{\psi}$)). The GRU in our model is primarily employed to capture temporal dependencies and relationships in the data. It's worth noting that while GRUs inherently transfer information across time steps in a sequence, this mechanism is distinct from the traditional concept of transfer learning, where pre-trained models are adapted for a different but related task. In the context of our model, the GRU's architecture, characterized by its reset and update gates, ensures the effective transfer of relevant information from one time step to the next within the same task. This internal "transfer" of information across time steps is pivotal for the model to make informed predictions based on both historical and current data.

Furthermore, our research explored both sequence-to-one (S2O) and sequence-to-sequence (S2S) predictions. Specifically, sequence-to-one (S2O) prediction involves processing a sequence of input data to produce a single output, while sequence-to-sequence (S2S) prediction takes a sequence of input data and predicts a corresponding output sequence, allowing for more dynamic and temporally structured predictions [48]. The examination of different sliding window lengths provides critical insights into the temporal influence on the prediction accuracy of the model. We utilized the last feature map of a CNN [17] to pro-

vide exteroceptive information of the environment to the prediction model. We argue that the incorporation of exteroceptive information from image streams provides long term correction data and thus will improve the sequence-to-sequence prediction capabilities. Besides the aforementioned sensor data we utilized the kinematic single-track model to compute the derivative, of the prediction target which is fed to the linear layer via the motion model. For this we transformed the formula Eq. 2.6 to derive $\dot{\beta}$, as seen in Eq. 4.1, by applying the assumption that $\cos(\beta) \approx 1$, and fed it as additional input to our GRU model thus creating a hybrid kinematic CNN-RNN model.

$$\dot{\beta} = \frac{a_y}{v} - \dot{\psi} \quad (4.1)$$

We argue that the proposed sensor suit is applicable for the use case due to the fact that (i) all new vehicles manufactured on or after May 1st, 2018 with a gross weight rating of 4536 kg or less are required to have a backup camera [49] and the general usage of cameras in vehicles increased by $\approx 315\%$ from 2014 to 2020 [50], (ii) GPS, IMU and CAN data is available in modern cars [51, 52].

We implemented the model using PyTorch [53] and Cuda 12.1. To train and test our model we collected a total of 110 min data on snow covered asphalt in the 3DCoAutoSim simulator [54]. Table 3 depicts an overview of the dataset composition. For the initial hyperparameter estimation, we relied on 3-fold cross-

Table 3
Dataset metrics

	Train	Validate
Samples	64501	1418
Minutes	107.39	2.21
$\mu(\beta)$	0.71	3.15
$\sigma(\beta)$	6.24	6.03

validation with 20 epochs, Table 4 visualizes the results and selected parameters. Besides the initially chosen hyperparameters we utilized learning rate scheduling based on *ReduceLROnPlateau*¹ to improve model performance and speed up the training process [55] [56]. Furthermore, to prevent overfitting we implemented early stopping when the validation loss did not decrease for 20% of the overall training epochs, L1-regularization ($\lambda = 0.001$), and 20% neuron dropout. Finally, we performed a train-test split of 75%-25%, and a separate dataset was recorded for the final evaluation.

Besides the proposed approach shown in Fig. 5, we compared our model in S2O and S2S prediction to the approach implemented in [8]. In all cases we used a separate validation dataset to evaluate our model that was neither used during training nor testing. Since the frequency of the sensors differed, we re-sampled the collected data, in preprocessing, to a frequency of 10 Hz. We then performed outlier removal, by relying on the z-score of 3, which indicates that data points beyond 3 standard deviations from the mean were considered as outliers, and further prepared the dataset in a sliding window approach as depicted in Table 5. Furthermore, we employed a feature scaling technique to normalize the range of the independent variables in the dataset as part of the data preprocessing step. The resulting dataset consisted of 65919 sample points valid for training, testing, and evaluation. Fig. 6 visualizes

¹Used to reduce learning rate when a metric has stopped improving https://pytorch.org/docs/stable/generated/torch.optim.lr_scheduler.ReduceLROnPlateau.html

Table 4

3 best validation scores of 3-fold cross validation. Best result in **bold**.

Hidden Dim	N Layers	Validation Score
64	2	0,0288
128	1	0,0266
128	2	0.0235

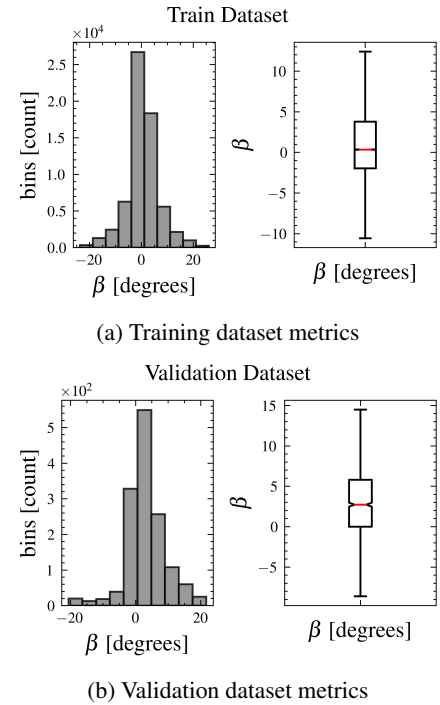


Fig. 6. Dataset metrics

the distribution of the ground truth VSA over the complete dataset.

4.4. Model Evaluation

In light of the correlation analysis, the highly non-linear feature processing within our proposed CNN pipeline, and the distinct correlation of front and rear camera features with the VSA, we pursued two distinct experimental approaches. These approaches not only included image data but also leveraged other sensor information as previously described in this section.

Table 5

Dataset structure for sequence-to-sequence prediction using a sliding window approach. The table represents input sequences with n features, spanning a window size of m time steps, leading up to the target output sequence of length p . Each row showcases how a target value y_{t+0} to y_{t+p} is paired with its corresponding input window. Specifically, for any target y_{t+0} , the corresponding input sequence is obtained by looking at $x_{1_{t-1}}$ to x_{n_t} and similarly for others.

y	x_1	...	x_n
y_{t+0}	$x_{1_{t-1}}$...	x_{n_t}
:	:	⋮	⋮
y_{t+p}	$x_{1_{t-m-1}}$...	$x_{n_{t-m-1}}$

Approach A utilized both front and rear image data in conjunction with the sensor data. This aimed to assess the combined impact of front and rear cameras and other sensor information on the model's VSA prediction capabilities.

On the other hand, Approach B focused exclusively on the front image data and the sensor information, intentionally omitting the rear image data. Despite using the same dataset as Approach A, Approach B truncated the rear camera information. The rationale behind this strategy was to test the relevance and impact of the rear camera data as suggested by the correlation analysis.

4.4.1. Sequence-to-One Prediction

To evaluate the precision of both models in the S2O prediction paradigm, we employed the symmetric mean absolute percentage error (sMAPE), as elaborated at the end of this Section. For the performance of our proposed hybrid CNN-GRU model on the task of S2O prediction we set during training the hyperparameter P to 1 and investigated the deviation from the ground truth (GT). To this end we evaluated 5 different S2O models with varying sliding window sizes $W = \{10, 20, 30, 50, 100\}$ as input. We compared both of our approaches, one with $W = 10$ and one with $W = 100$ against the baseline model of [8]. The primary motivation for using differential plots was their natural capacity to assist an easy and quick understanding of the mismatch in prediction outputs relative to the ground truth, we further chose to visualize sliding window sizes on both ends of our spectrum to depict the difference in accuracy.

4.4.2. Sequence-to-Sequence Prediction

Given the interdependent nature of the VSA data, which dynamically evolves based on past, present, and future states, the S2S prediction paradigm is integral to our models, designed to capture and interpret the complex temporal dependencies that exist among different states in a sequence, thereby producing accurate estimations of future vehicle side-slip angles.

To evaluate the effectiveness of our S2S models, we conducted a series of comparative analyses using different prediction horizons. We employed the sSMAPE as our performance metric, providing a robust measure of the prediction accuracy of our models across various time horizons $P = \{10, 20, 30, 100\}$.

The outcomes yielded by our two experimental strategies in relation to the two distinct prediction paradigms, S2O and S2S, are delineated in sections 5.2 and 5.3, respectively. To further fine-tune our models, we trained them using an array of hyperparameter

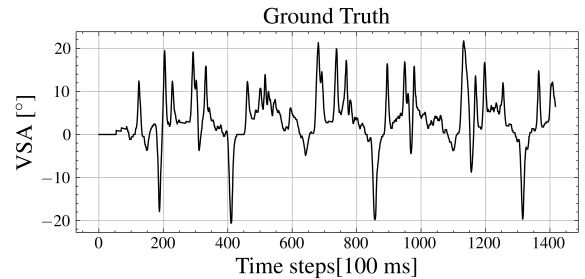


Fig. 7. Ground truth VSA of the evaluation dataset.

combinations, these encompassed various sliding window input sizes $W = \{10, 20, 30, 50, 100\}$ and a spectrum of prediction horizons $P = \{1, 10, 20, 30, 100\}$. The GT values of the evaluation dataset can be seen in Fig. 7.

Finally, we evaluated the model performance using the sMAPE, sequence wise sMAPE (sSMAPE) as well as the averaged sSMAPE (\bar{E}).

sMAPE

For evaluating the models' accuracy we relied on sMAPE, the most commonly used metric to determine the accuracy of time sequence predictions [57]. Further, the sMAPE metric is especially suited for forecasting problems, as it provides a symmetric, scale-independent error measure, which is particularly useful when dealing with datasets that may contain zeros, as seen in Eq. 4.2 [58].

$$sMAPE = \frac{2}{n} \sum_1^n \frac{|y_i - \hat{y}_i|}{\max(|y_i| + |\hat{y}_i|, \epsilon)}, \quad (4.2)$$

being y_i the current target value, \hat{y}_i the current prediction value, and ϵ a constant to avoid division by 0. Lower values of sMAPE indicate higher precision in the predictions.

Sequence Wise sMAPE

In our computation, we applied Eq. 4.2 to the predictions generated by our sequence-to-one/sequence model. Given that our model produced a set of sequences as its prediction output, the calculation was done on a per-sequence basis over all time steps and subsequently divided by the total number of time steps, yielding the sMAPE per sequence sSMAPE (sequence wise sMAPE) as described in Eq. 4.3:

Table 6

Statistical investigation of the relation of the PCA-based processed CNN features of the front and rear camera to β . The first principal components (latent dimensions) corresponding to the highest projected variance are shown. We utilized Pearson's correlation and Spearman's rank correlation to analyze the association between the variables. The results provided evidence against the null hypotheses for the front camera. Conversely, these findings were minor for the rear camera.

PCA dimension	Front				Rear			
	Pearson's corr.		Spearman's rank corr.		Pearson's corr.		Spearman's rank corr.	
	Estimate	p-value	Estimate	p-value	Estimate	p-value	Estimate	p-value
1	-0.0566	<1e-4	-0.0352	0.0006	0.0615	<1e-4	0.0686	<1e-4
2	0.1951	<1e-4	0.1800	<1e-4	0.0816	<1e-4	0.1268	<1e-4
3	-0.5244	<1e-4	-0.6290	<1e-4	-0.0408	<1e-4	-0.1000	<1e-4
4	0.0876	<1e-4	0.1119	<1e-4	-0.033	0.0013	0.0037	0.7144
5	0.2232	<1e-4	0.2095	<1e-4	-0.0546	<1e-4	-0.0291	0.0048

$$sSMAPE = \frac{2}{n \cdot N} \sum_{i=1}^N \sum_{t=1}^n \frac{|y_{i,t} - \hat{y}_{i,t}|}{\max(|y_{i,t}| + |\hat{y}_{i,t}|, \epsilon)}, \quad (4.3)$$

In this equation, $y_{i,t}$ is the true value for the i -th sequence at time step t over all data points n , and $\hat{y}_{i,t}$ represents the predicted value for the i -th sequence at time step t . The inner sum calculates the sMAPE for each sequence i , and the outer sum averages these values over all sequences N to compute the sMAPE per sequence. We used the *sSMAPE metric*, as it evaluates the model on a per-sequence basis, which is more appropriate for S2S models than treating the entire output as one input. The method was then capable of capturing errors that were specific to individual sequences.

Averaged sSMAPE

To provide a comprehensive overview of the performance of the models, we averaged the error metrics across all prediction sequences. This *mean* error, as seen in Eq. 4.4, represented the overall performance of the models across different prediction horizons and offered a summary measure of their accuracy.

$$\bar{E} = \frac{1}{P} \sum_{i=1}^N sSMAPE_i, \quad (4.4)$$

where P represents the total number of sequences (prediction horizon), and $sSMAPE_i$ (sequence wise sMAPE) denotes the error value for the i -th prediction horizon sequence.

5. Results

This section describes the results of the relationship analysis of CNN image features and the VSA β as well as a comparative overview of the performance of our proposed models against the baseline model proposed in [8]² for the side-slip angle estimation on two prediction paradigms: Sequence-to-One (S2O) and Sequence-to-Sequence (S2S).

5.1. Correlation Analysis

Table 6 reports the detailed findings of the correlation analysis described in 4.2, summarizing the estimated correlation values and their associated p-values for both Pearson's and Spearman's rank correlation methods. Each row represents one of the principal components from the PCA-based processed CNN features. Each column shows the estimate and p-value of the respective correlation method for both the front and rear cameras.

5.2. Sequence-to-One Prediction Model Evaluation

Fig. 8 showcases the effectiveness of our hybrid CNN-GRU model in executing the S2O prediction task. It presents comparative differential plots for both Approach A and Approach B under different sliding window lengths of $W = 10$ and $W = 100$. The divergence from the ground truth provides an insightful measure of the prediction accuracy of both approaches.

²We had to implement a minor modification on the output regression head so that the model could also be used for S2S prediction.

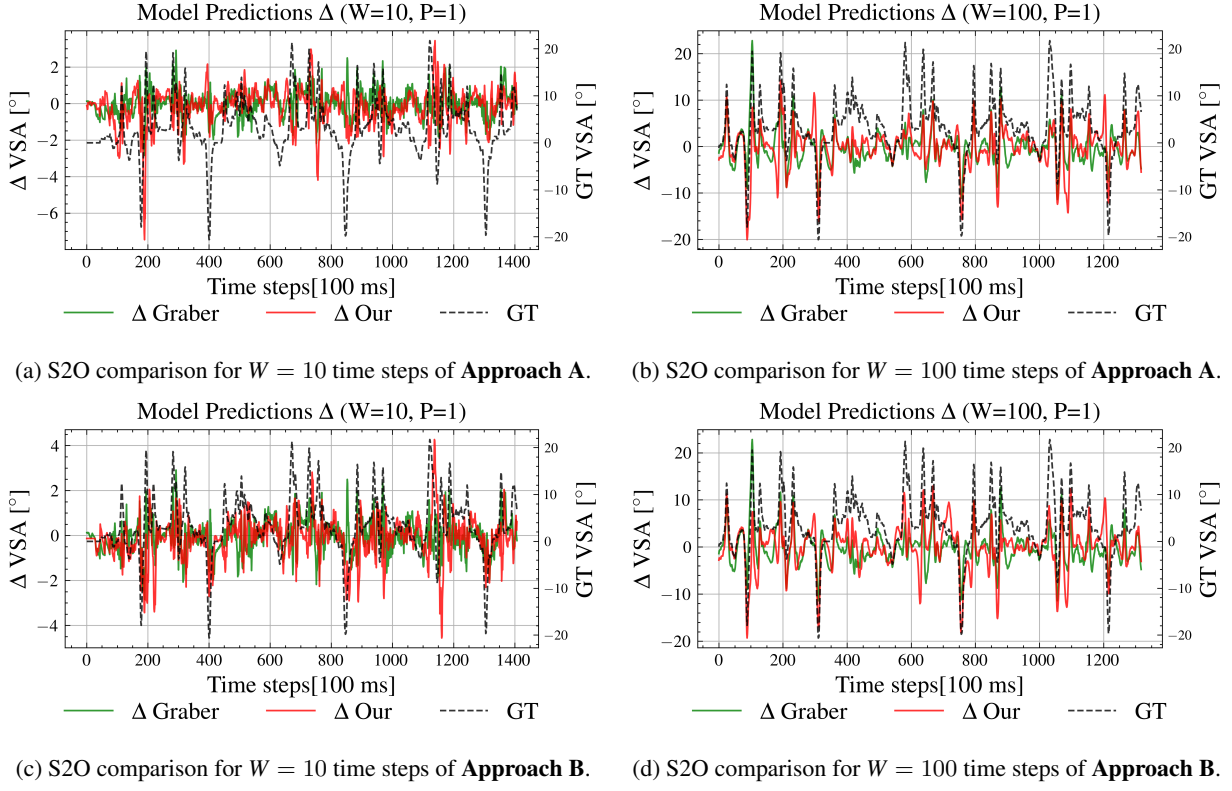


Fig. 8. Comparative differential plots of S2O predictions from **Approach A** (middle) and **Approach B** (bottom), showing deviation from ground truth. Different input window lengths of $W = 10$ and $W = 100$ are represented, highlighting the temporal influence on prediction accuracy.

The examination of these different sliding window lengths provides critical insights into the temporal influence on the prediction accuracy of the model. In our model training, we settled on 20 epochs based on preliminary experiments. Beyond this, we noticed an increase in validation loss, hinting at overfitting. While the ideal epoch count can vary with the dataset, for ours, 20 epochs ensured a balance between computational efficiency and model performance. As previously mentioned, the performance metric, *sSMAPE*, was employed to evaluate the model's effectiveness in the S2O prediction paradigm. The calculated values are documented in Table 7, that provides a comparative overview of the S2O prediction outcomes of the various models. For a complete overview of the differential plots for all window sizes $W = \{10, 20, 30, 50, 100\}$, refer to Appendix A, it provides a collection of plots for both Approach A (Fig. 10) and Approach B (Fig. 11), which encapsulate the variability of each models' performance across a broad range of temporal sliding input windows.

In Fig. 8a and 8c we can see that, compared to the ground truth and the approach of [8], our models generated similar accurate results, except for cases when the target value is close to the min/max values of the training data, e.g. as seen at ≈ 180 ms. For larger input sizes, as seen in Fig. 8b and 8d, it is apparent that the deviation from the GT was significantly higher for all three models. The largest deviations of the GT for the models with $W = 100$ were close to the min/max

Table 7

sSMAPE compared to ground truth for $P = 1$ time step. Approach A uses all features, Approach B does not use rear image features, and [8] is the baseline model used for comparison. Best result in **bold**.

Window Size	Approach A	Approach B	[8]
10	0.410	0.387	0.366
20	0.373	0.340	0.335
30	0.376	0.318	0.454
50	0.741	0.778	0.478
100	0.783	0.827	0.754

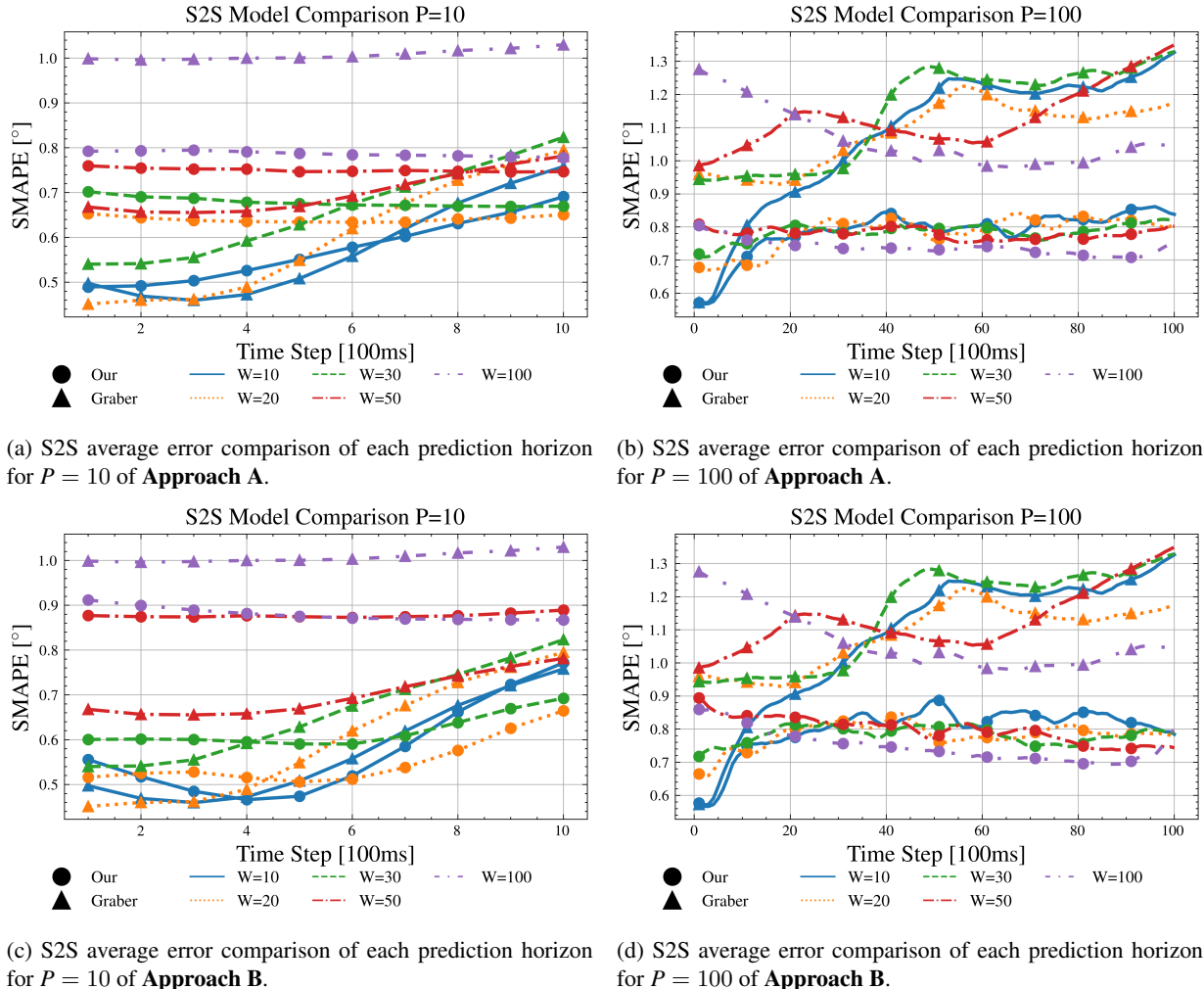


Fig. 9. S2S sMAPE comparison for each individual prediction horizon sequence

values of our training just like for the models with $W = 10$.

5.3. Sequence-to-Sequence Prediction Model Evaluation

Fig. 9 presents the outcomes of applying the S2S prediction paradigm, illustrating the sMAPE metric at each prediction horizon. For a more granular perspective see Table 8, as it displays the mean sMAPE \bar{E} for respective prediction horizons $P = \{10, 20, 30, 100\}$. It visualizes the results of a comparative analysis of mean sMAPE across varying prediction horizons, focusing on our proposed Approach A, Approach B, and the model established by [8]. The results reflect the performance of the S2S models in capturing and

interpreting complex temporal dependencies existing among different states in a sequence, and accordingly, generating accurate estimations of future vehicle states.

The comparison of S2S averaged sMAPE for each individual prediction sequence for different horizons P between Approach A (Fig. 12) and Approach B is illustrated in the Appendix B (Fig. 13).

The comparison of the S2S prediction paradigms is demonstrated through Fig. 9, which illustrates the sMAPE for each prediction horizon. The results for $P = 10$ and $P = 100$ at the initial prediction time step indicate that the model proposed by [8] consistently displays lower sMAPE values than Approach A and Approach B in 9 out of 20 cases. Additionally, an increased window size correlates with an increment

Table 8

Comparison of Average Errors (\bar{E}) for different sliding window sizes in Sequence-to-Sequence prediction. The table is divided into four sections based on prediction horizon (P). Each section compares the performance of Approach A, Approach B, and the benchmark model [8] for varying window sizes $W = \{10, 20, 30, 50, 100\}$. The best-performing method for each window size is highlighted in **bold**.

Prediction Horizon	Window Size	Approach A	Approach B	[8]
$P = 10$	10	0.572	0.576	0.574
	20	0.641	0.551	0.599
	30	0.679	0.6819	0.660
	50	0.750	0.877	0.700
	100	0.787	0.880	1.007
$P = 20$	10	0.645	0.673	0.737
	20	0.672	0.674	0.719
	30	0.731	0.800	0.739
	50	0.807	0.835	0.780
	100	0.794	0.820	0.999
$P = 30$	10	0.685	0.693	0.805
	20	0.721	0.717	0.835
	30	0.757	0.778	0.863
	50	0.827	0.815	0.845
	100	0.756	0.788	1.031
$P = 100$	10	0.788	0.802	1.084
	20	0.786	0.782	1.085
	30	0.785	0.783	1.149
	50	0.780	0.799	1.131
	100	0.783	0.748	1.064

in the *sSMAPE* across all models. The last prediction step, however, exhibits a different trend with the baseline model of [8] scoring lower *sSMAPE* values only on 2 out of 20 prediction sequences.

When comparing Approach A with Approach B, results for the first prediction step show Approach A surpassing Approach B only in 2 out of 5 instances when $P = 100$, specifically for window sizes of $W = 20$ and $W = 30$. A similar pattern is observed for $P = 10$, where Approach A outperforms B only twice, again at window sizes of $W = 20$ and $W = 30$. Therefore, for the initial prediction step, Approach B holds the superior record 60% of the time.

For the last prediction step, the dynamics shift somewhat. Approach A surpasses Approach B in 4 out of 5 cases when $P = 100$, spanning all window sizes except $W = 100$. For $P = 10$, however, Approach A does not outperform Approach B in any instance. Consequently, for the last prediction step, Approach A proves superior in 4 out of 10 cases.

Another point of comparison is the fluctuation of the *sSMAPE* over time. As depicted in Fig. 9a and 9c, our models generally exhibit an initial decrease in the *sSMAPE* which eventually increases after reaching a minimum. In contrast, the model of [8] holds a stable *sSMAPE* for the early time steps, followed by an increase. This observation suggests that both our models surpass the model of [8] in long-term predictions, with the exact intersection point varying based on the window size W . Specifically, for the window size $W = 100$, both our models demonstrate a steeper *sSMAPE* as compared to the model of [8], which shows a continual increase of the *sSMAPE* across all window sizes except for $W = 100$.

Finally, the models were compared based on their average *sSMAPE* (\bar{E}) across various prediction horizons. Table 8 provided the mean *sMAPE* for the prediction horizons $P = \{10, 20, 30, 100\}$ for Approach A, Approach B, and the model by [8].

6. Discussion

6.1. Correlation Analysis

The results of the correlation analysis presented in Table 6 demonstrate several key insights regarding the relationship between PCA-based processed CNN features of the front and rear camera to β . A detailed investigation of these results is provided below.

High correlations are observed in the second, third, and fifth latent dimensions with β for the front camera, as demonstrated by Pearson's correlation coefficients of 0.1951, -0.5244, and 0.2232, respectively.

These results are echoed by the Spearman's rank correlation, suggesting that these statistical relationships are robust. The third latent dimension, in particular, shows a negative correlation, implying an inverse relationship with the VSA in this dimension. The first and fourth latent dimensions also display correlations significant at $\alpha = 0.001$, strongly refuting the null hypotheses $H_{0,Pearson}$ and $H_{0,Spearman}$.

The correlations for the rear camera present a different narrative, being notably lower across all latent dimensions compared to the front camera. Nevertheless, most latent dimensions still display statistical significance at $\alpha = 0.001$. An exception is found in the fourth dimension, which demonstrates a non-significant correlation in the Spearman's rank correlation test, suggesting that this dimension's relationship might not be robust or meaningful.

6.2. Sequence-to-One Prediction

Based on the results of the S2O prediction paradigm we recognize the need for a more in-depth exploration of our model's capacity. We recognize that (*i*) additional data augmentation or an expanded training dataset may be necessary for superior data extrapolation. This realization emerged as we compared our approach to that of [8]. On the other hand, (*ii*) the divergence could also be rooted in the different methodologies for feature extraction from sensor data between our model and [8]'s. Furthermore, (*iii*) our model extends beyond the approach of [8] by incorporating exteroceptive sensor data, specifically image streams from vehicle cameras processed via CNN. Consequently, our CNN-GRU model captures a different spectrum of information for predicting the extremes of the VSA compared to a standalone GRU. This divergence may contribute to reduced accuracy near the extreme values of the training data. As we continue to refine our model, adjustments to the CNN and the inclusion of supplementary data sources are avenues we plan to explore for improving accuracy.

6.3. Sequence-to-Sequence Prediction

Approach A seems to be slightly more beneficial, especially for window sizes $W = 20$ and $W = 30$. However, if the interest lies in the final prediction step with a horizon of $P = 100$, Approach A might be preferred due to its superior performance in most instances. Another factor to consider is the stability of the *sSMAPE* over time, where both our models showcase a stronger performance than [8]'s model for larger window sizes. These observations suggest that our models may offer an advantage for applications requiring long-term predictions.

It is worth noting that Approach A surpassed Approach B in 13 out of 25 cases. This indicates that notwithstanding the diminished correlation of the rear camera features with the side-slip angle, these features nonetheless deliver consequential information that augments the prediction accuracy of our model. The origin of this discrepancy may be rooted in various elements. First and foremost, the nexus between the rear camera features and the side-slip angle could be non-linear and intricate, reducing its detectability by conventional correlation measures but can still be deciphered by state-of-the-art prediction models such as deep neural networks. The sophisticated architecture of such models enables them to extract latent,

non-linear patterns in data, thereby enhancing prediction performance even in the absence of an evident linear relationship. Secondly, an overlooked aspect in the correlation analysis is the potential synergistic effect among different data types. In this scenario, the interaction of rear camera features with other pieces of information, such as front camera features or steering angle, could substantially enrich the predictive capacity of the model. This collective effect is not discernible by examining individual correlation coefficients, which provide a somewhat simplistic view of the relationship between individual variables and the target. Lastly, it is plausible that the rear camera features serve as particularly vital information in specific circumstances, for instance, when the vehicle is reversing or during a sharp turn. Such contextual utility of rear camera features contributes to a comprehensive, more accurate prediction across a variety of situations. Taken together, these observations highlight the importance of including diverse types of data in complex prediction tasks, even those with seemingly low correlation to the target variable. It underlines the multifaceted nature of data utility in model performance and cautions against over-reliance on individual correlation measures when making decisions about feature inclusion. The analysis thus suggests the potential benefit of leveraging machine learning models capable of capturing both linear and non-linear relationships and interactions among features.

Compared to the baseline model of [8] both of our models outperformed it for longer prediction horizons (≥ 2 s). Especially Approach A demonstrated the best results for prediction horizons of two and three seconds, while Approach B outperformed Approach A on a prediction horizon of 10 seconds. This may be attributed to the model structure of Approach A that may be too complex for the little training data, leading to less accurate predictions. Therefore, Approach B, which is a smaller model, was better suited for longer prediction horizons as it was able to generalize better on the limited dataset.

7. Conclusion and Future Research

In this work we presumed that the incorporation of CNN features from the cameras of a car can besides the normally utilized kinematic and dynamic parameters improve the estimation of the side-slip angle. Our statistical analysis results revealed a significant relationship between the second, third, and fifth latent di-

mensions of the front camera and the side-slip angle (denoted as β) but not of the rear camera. This outcome strongly supports our assumption, demonstrating the potential of our approach for side-slip angle estimation. In contrast, the rear camera features showed a low correlation with β , suggesting that they might not contribute significantly to the model's performance. These findings provide substantial guidance for future research directions. Nonlinear correlations could be explored in future studies, or alternative dimensionality reduction techniques could be employed to uncover hidden patterns and relationships. Further analysis beyond the first five principal components might also yield additional insights into the image data and VSA relationship.

Contrary to the correlation analysis results, our empirical investigation, relying on our hybrid CNN-GRU, illuminated that exploiting all available features (Approach A) often led to superior side-slip angle predictions relative to utilizing all features excluding the rear camera features (Approach B).

Our investigation concentrated on three principal areas: correlation analysis, sequence-to-one prediction, and sequence-to-sequence prediction. In section 4.2 we explored the relationships between latent variables inherent to the front and rear image features and the VSA β . Transitioning to the sequence-to-one prediction we conducted an evaluation, juxtaposing our two unique prediction methodologies against a benchmark model. The outcome revealed that both our approaches showed substantial promise. In the final part of our analysis, the sequence-to-sequence prediction, we evaluated the proficiency of our models in the demanding task of predicting future sequences based on prior ones. Our analysis furnished intriguing revelations. Although we based our work on different design paradigms all our models provided comparable results revealing certain advantages in terms of temporal prediction demands of the application.

The insights gained from these results contribute to a wider understanding as they do not only highlight the efficacy of our proposed models but also underscore potential limitations, particularly in utilizing the S2S prediction paradigm in VSA estimation. The real-world applicability of our model is evident in its potential to improve vehicle control in adverse conditions like snow. Its strength in longer prediction horizons makes it valuable for autonomous driving systems, where precise side-slip angle estimation is crucial for safety. The model's ability to integrate diverse sensor data also adds contextual adaptability, useful in

specific driving scenarios such as reversing or sharp turns.

Future research is needed to confirm these results and should consider integrating attention mechanisms and encoder-decoder structures into the model. Attention mechanisms could enhance feature relevance at each time step, potentially improving prediction accuracy. Moreover, encoder-decoder or autoencoder structures might enhance performance for larger input window sizes and prediction horizons, as they are adept at capturing temporal dependencies in sequence-to-sequence prediction tasks. These adjustments could offer a promising avenue for model performance improvement in side-slip angle prediction. In addition to the aforementioned avenues for future research, it may be beneficial to explore different CNN architectures to optimize VSA estimation. This could include direct estimation as well as the use of temporally contiguous gray-scale images. Ablation studies could help to isolate the effects of each architectural component and input modality and separate projection layers for each input could offer more flexibility in learning the weights and biases for each input. Moreover, investigating the use of sensors to dynamically determine the most suitable approach based on conditional probabilities and safety conditions could provide a more adaptive and robust system for VSA estimation on real systems. Finally, considering different hybrid models tailored to specific input states might optimize a first step towards real-time performance of the hybrid model. As an alternative to the current use of PCA for dimensionality reduction, future research could consider other dimensionality reduction methods such as [59] for discovering the most effective feature spaces and optimizing the number of features. This could provide a more robust and accurate approach for VSA estimation.

References

- [1] Robert Bosch GmbH [homepage on the Internet]. Vehicle dynamics control 2.0.; 2022 [updated 2022; cited 2022 Dec 16]. Available from: <https://www.bosch-mobility.com/en/solutions/driving-safety/vehicle-dynamics-control/>.
- [2] Chindamo D, Lenzo B, Gadola M. On the vehicle sideslip angle estimation: A literature review of methods, models, and innovations. Applied Sciences (Switzerland). 2018;8(3).
- [3] Liu J, Wang Z, Zhang L, Walker P. Sideslip angle estimation of ground vehicles: A comparative study. IET Control Theory and Applications. 2020;14(20):3490-505.
- [4] Essa MG, Elias CM, Shehata OM. Comprehensive Performance Assessment of Various NN-based Side-Slip Angle Estimators (ANN-SSE). In: 2021 IEEE 93rd Vehicular Technology Conference (VTC2021-Spring); 2021. p. 1-6.

- [5] Rajamani R. Lateral vehicle dynamics. In: Vehicle Dynamics and control. Springer; 2012. p. 15-46, 201-3.
- [6] Biase FD, Lenzo B, Timpone F. Vehicle Sideslip Angle Estimation for a Heavy-Duty Vehicle via Extended Kalman Filter Using a Rational Tyre Model. *IEEE Access*. 2020;8:142120-30.
- [7] Kim D, Kim G, Choi S, Huh K. An integrated deep ensemble-unscented Kalman filter for sideslip angle estimation with sensor filtering network. *IEEE Access*. 2021;9:149681-9.
- [8] Gruber T, Lupberger S, Unterreiner M, Schramm D. A Hybrid Approach to Side-Slip Angle Estimation with Recurrent Neural Networks and Kinematic Vehicle Models. *IEEE Transactions on Intelligent Vehicles*. 2019;4(1):39-47.
- [9] Kong D, Wen W, Zhao R, Lv Z, Liu K, Liu Y, Gao Z. Vehicle lateral velocity estimation based on long short-term memory network. *World Electric Vehicle Journal*. 2022;13(1).
- [10] Liu Y, Morales-Alvarez W, Novotny G, Olaverri-Monreal C. Study of ROS-Based Autonomous Vehicles in Snow-Covered Roads by Means of Behavioral Cloning Using 3DCoAutoSim. *Lecture Notes in Networks and Systems*. 2022;470 LNNS:211-21.
- [11] Bebis G, Georgopoulos M. Feed-forward neural networks. *IEEE Potentials*. 1994;13(4):27-31.
- [12] Rumelhart DE, McClelland JL. Learning Internal Representations by Error Propagation. In: Learning Internal Representations by Error Propagation. MIT Press; 1987. p. 318-62.
- [13] Cho K, van Merriënboer B, Bahdanau D, Bengio Y. On the properties of neural machine translation: Encoder-decoder approaches. In: Proceedings of SSST 2014 - 8th Workshop on Syntax, Semantics and Structure in Statistical Translation. Association for Computational Linguistics (ACL); 2014. p. 103-11.
- [14] Hochreiter S, Schmidhuber J. Long Short-Term Memory. *Neural Computation*. 1997;9(8):1735-80.
- [15] Carranza-García M, Galán-Sales FJ, Luna-Romera JM, Riquelme JC. Object detection using depth completion and camera-LiDAR fusion for autonomous driving. *Integrated Computer-Aided Engineering*. 2022;29(3):241-58.
- [16] Hüpen P, Kumar H, Shymanskaya A, Swaminathan R, Habbel U. Impulsivity Classification Using EEG Power and Explainable Machine Learning. *International Journal of Neural Systems*. 2023;33(02):2350006. PMID: 36632032. Available from: <https://doi.org/10.1142/S0129065723500065>.
- [17] Szegedy C, Liu W, Jia Y, Sermanet P, Reed S, Anguelov D, Erhan D, Vanhoucke V, Rabinovich A. Going deeper with convolutions. In: Proceedings of the IEEE conference on computer vision and pattern recognition; 2015. p. 1-9.
- [18] Pett MA. Nonparametric statistics for health care research: Statistics for small samples and unusual distributions. Sage Publications; 2015.
- [19] Bishop CM, Nasrabadi NM. Pattern recognition and machine learning. vol. 4. Springer; 2006.
- [20] Albawi S, Mohammed TA, Al-Zawi S. Understanding of a convolutional neural network. In: Proceedings of 2017 International Conference on Engineering and Technology, ICET 2017. vol. 2018-Janua. Institute of Electrical and Electronics Engineers Inc.; 2018. p. 1-6.
- [21] Alom MZ, Taha TM, Yakopcic C, Westberg S, Sidike P, Nasrin MS, Hasan M, Van Essen BC, Awwal AAS, Asari VK. A State-of-the-Art Survey on Deep Learning Theory and Architectures. *Electronics* 2019, Vol 8, Page 292. 2019 3(3):292. Available from: <https://www.mdpi.com/2079-9292/8/3/292> <https://www.mdpi.com/2079-9292/8/3/292>.
- [22] Dieter Schramm Manfred Hiller RBa. Vehicle Dynamics: Modeling and Simulation. 2nd ed. Springer; 2018.
- [23] Jazar RN. Vehicle dynamics: theory and application. Springer; 2017.
- [24] Farah S, David A W, Humaira N, Aneela Z, Steffen E. Short-term multi-hour ahead country-wide wind power prediction for Germany using gated recurrent unit deep learning. *Renewable and Sustainable Energy Reviews*. 2022 10;167:112700.
- [25] Sachin S, Tripathi A, Mahajan N, Aggarwal S, Nagrath P. Sentiment Analysis Using Gated Recurrent Neural Networks. *SN Computer Science*. 2020 Mar;1(2):74. Available from: <https://doi.org/10.1007/s42979-020-0076-y>.
- [26] Wazrah AA, Alhumoud S. Sentiment Analysis Using Stacked Gated Recurrent Unit for Arabic Tweets. *IEEE Access*. 2021;9:137176-87. Available from: <https://www.kaggle.com/monsterspy/conv-lstm-sentiment-analysis->.
- [27] Wöber W, Curto M, Tibihika P, Meulenbroek P, Alemayehu E, Mehnen L, Meimberg H, Sykacek P. Identifying geographically differentiated features of Ethopian Nile tilapia (*Oreochromis niloticus*) morphology with machine learning. *PLOS ONE*. 2021;16(4):1-30. Available from: <https://doi.org/10.1371/journal.pone.0249593>.
- [28] Yin W, Kann K, Yu M, Schütze H. Comparative Study of CNN and RNN for Natural Language Processing. *arXiv*. 2017. Available from: <http://arxiv.org/abs/1702.01923>.
- [29] Shewalkar A, Nyavanandi D, Ludwig SA. Performance Evaluation of Deep neural networks Applied to Speech Recognition: Rnn, LSTM and GRU. *Journal of Artificial Intelligence and Soft Computing Research*. 2019 10;9(4):235-45. Available from: <https://www.infona.pl/resource/bwmeta1.element.baztech-0106e25d-92b6-4c93-8317-367a9f574578>.
- [30] Chung J, Gülcehrə Ç, Cho K, Bengio Y. Empirical Evaluation of Gated Recurrent Neural Networks on Sequence Modeling. *CoRR*. 2014;abs/1412.3555. Available from: <http://arxiv.org/abs/1412.3555>.
- [31] Farahani A, Pourshojae B, Rasheed K, Arabnia HR. A Concise Review of Transfer Learning. *CoRR*. 2021;abs/2104.02144. Available from: <https://arxiv.org/abs/2104.02144>.
- [32] Polack P, Alché F, d'Andréa Novel B, de La Fortelle A. The kinematic bicycle model: A consistent model for planning feasible trajectories for autonomous vehicles? In: 2017 IEEE Intelligent Vehicles Symposium (IV); 2017. p. 812-8.
- [33] Corke P. Robotics, Vision and Control. vol. 118 of Springer Tracts in Advanced Robotics. Cham: Springer Cham; 2017. Available from: <http://link.springer.com/10.1007/978-3-319-54413-7>.
- [34] LeCun Y, Bengio Y, Hinton G. Deep learning. *nature*. 2015;521(7553):436-44.
- [35] Melzi S, Resta F, Sabbioni E. Vehicle sideslip angle estimation through neural networks: application to numerical data. In: Engineering Systems Design and Analysis. vol. 42495; 2006. p. 167-72.
- [36] Sieberg PM, Blume S, Harnack N, Maas N, Schramm D. Hybrid State Estimation Combining Artificial Neural Network and Physical Model. 2019 IEEE Intelligent Transportation Systems Conference (ITSC). 2019:894-9.
- [37] Sajjad M, Khan ZA, Ullah A, Hussain T, Ullah W, Lee MY, Baik SW. A Novel CNN-GRU-Based Hybrid Approach for Short-Term Residential Load Forecasting. *IEEE Access*. 2020;8:143759-68.

- [38] Hasannezhad M, Ouyang Z, Zhu WP, Champagne B. An Integrated CNN-GRU Framework for Complex Ratio Mask Estimation in Speech Enhancement. 2020 Asia-Pacific Signal and Information Processing Association Annual Summit and Conference, APSIPA ASC 2020 - Proceedings. 2020:764-8.
- [39] Yu J, Zhang X, Xu L, Dong J, Zhangzhong L. A hybrid CNN-GRU model for predicting soil moisture in maize root zone. Agricultural Water Management. 2021;245(June 2020):106649. Available from: <https://doi.org/10.1016/j.agwa.2020.106649>.
- [40] Li E, Zhou J, Yang C, Wang M, Li Z, Zhang H, Jiang T. CNN-GRU network-based force prediction approach for variable working condition milling clamping points of deformable parts. International Journal of Advanced Manufacturing Technology. 2022;119(11-12):7843-63. Available from: <https://doi.org/10.1007/s00170-021-08520-2>.
- [41] Ma C, Zhao Y, Dai G, Xu X, Wong SC. A Novel STFSA-CNN-GRU Hybrid Model for Short-Term Traffic Speed Prediction. IEEE Transactions on Intelligent Transportation Systems. 2022.
- [42] Hussein A, Diaz-Alvarez A, Armingol JM, Olaverri-Monreal C. 3DCoAutoSim: Simulator for Cooperative ADAS and Automated Vehicles. IEEE Conference on Intelligent Transportation Systems, Proceedings, ITSC. 2018 12;2018-November:3014-9.
- [43] Certad N, Morales-Alvarez W, Novotny G, Olaverri-Monreal C. JKU-ITS automobile for research on autonomous vehicles. In: International Conference on Computer Aided Systems Theory. Springer; 2022. p. 329-36.
- [44] BoneCracker Games [homepage on the Internet]. Realistic Car Controller | Physics | Unity Asset Store. Unity Technologies; 2023. 2023 [updated 2023 Jul 23; cited 2023 Jul 30]. Available from: <https://assetstore.unity.com/packages/tools/physics/realistic-car-controller-16296>.
- [45] Lapuschkin S, Wäldchen S, Binder A, Montavon G, Samek W, Müller KR. Unmasking Clever Hans predictors and assessing what machines really learn. Nature communications. 2019;10(1):1096.
- [46] Tian Y, Ding C, Lin YF, Ma S, Li L. Automatic feature type selection in digital photogrammetry of piping. Computer-Aided Civil and Infrastructure Engineering. 2022;37(10):1335-48. Available from: <https://onlinelibrary.wiley.com/doi/abs/10.1111/mice.12840>.
- [47] Graña M, Silva M. Impact of Machine Learning Pipeline Choices in Autism Prediction From Functional Connectivity Data. International Journal of Neural Systems. 2021;31(04):2150009. PMID: 33472548. Available from: <https://doi.org/10.1142/S012906572150009X>.
- [48] Brownlee J. Deep learning for time series forecasting: predict the future with MLPs, CNNs and LSTMs in Python. Machine Learning Mastery; 2018.
- [49] Huntley, Mike. Federal motor vehicle safety standard no. 111, Rear Visibility; 2019. Available from: <https://www.federalregister.gov/documents/2019/10/10/2019-22036/federal-motor-vehicle-safety-standard-no-111-rear-visibility>.
- [50] Statista Inc [homepage on the Internet]. Worldwide shipments of cameras for cars in between 2014 and 2020 (in million units); 2022. 2023 [updated 2023 Jan 6; cited 2023 Jul 15]. Available from: <https://www.statista.com/statistics/262015/worldwide-shipments-of-cameras-for-cars/>.
- [51] Campbell S, O'Mahony N, Kralcova L, Riordan D, Walsh J, Murphy A, Ryan C. Sensor Technology in Autonomous Vehicles : A review. In: 2018 29th Irish Signals and Systems Conference (ISSC); 2018. p. 1-4.
- [52] Varghese JZ, Boone RG, others. Overview of autonomous vehicle sensors and systems. In: International Conference on Operations Excellence and Service Engineering. sn; 2015. p. 178-91.
- [53] Paszke A, Gross S, Massa F, Lerer A, Bradbury J, Chanan G, Killeen T, Lin Z, Gimelshein N, Antiga L, Desmaison A, Köpf A, Yang E, DeVito Z, Raison M, Tejani A, Chilamkurthy S, Steiner B, Fang L, Bai J, Chintala S. PyTorch: An Imperative Style, High-Performance Deep Learning Library. Advances in Neural Information Processing Systems. 2019 12;32. Available from: <https://arxiv.org/abs/1912.01703v1>.
- [54] Olaverri-Monreal C, Errea-Moreno J, Díaz-Álvarez A, Biurrun-Quel C, Serrano-Arriezu L, Kuba M. Connection of the SUMO microscopic traffic simulator and the unity 3D game engine to evaluate V2X communication-based systems. Sensors. 2018;18(12):4399.
- [55] Konar J, Khandelwal P, Tripathi R. Comparison of Various Learning Rate Scheduling Techniques on Convolutional Neural Network. 2020 IEEE International Students' Conference on Electrical, Electronics and Computer Science, SCEECS 2020. 2020 2.
- [56] Fernández-Rodríguez JD, Palomo EJ, Ortiz-de Lazcano-Lobato JM, Ramos-Jiménez G, López-Rubio E. Dynamic learning rates for continual unsupervised learning. Integrated Computer-Aided Engineering. 2023;30:257-73. 3. Available from: <https://doi.org/10.3233/ICA-230701>.
- [57] Martínez F, Charre F, Frías MP, Martínez-Rodríguez AM. Strategies for time series forecasting with generalized regression neural networks. Neurocomputing. 2022 6;491:509-21.
- [58] PyTorch Foundation [homepage on the Internet]. Symmetric Mean Absolute Percentage Error. Lightning-AI; 2023. 2023 [updated 2023; cited 2023 Jul 15]. Available from: https://torchmetrics.readthedocs.io/en/stable/regression/symmetric_mean_absolute_percentage_error.html.
- [59] Rafiei MH, Adeli H. A New Neural Dynamic Classification Algorithm. IEEE Transactions on Neural Networks and Learning Systems. 2017;28(12):3074-83.

Appendix A. S2O Differential Plots

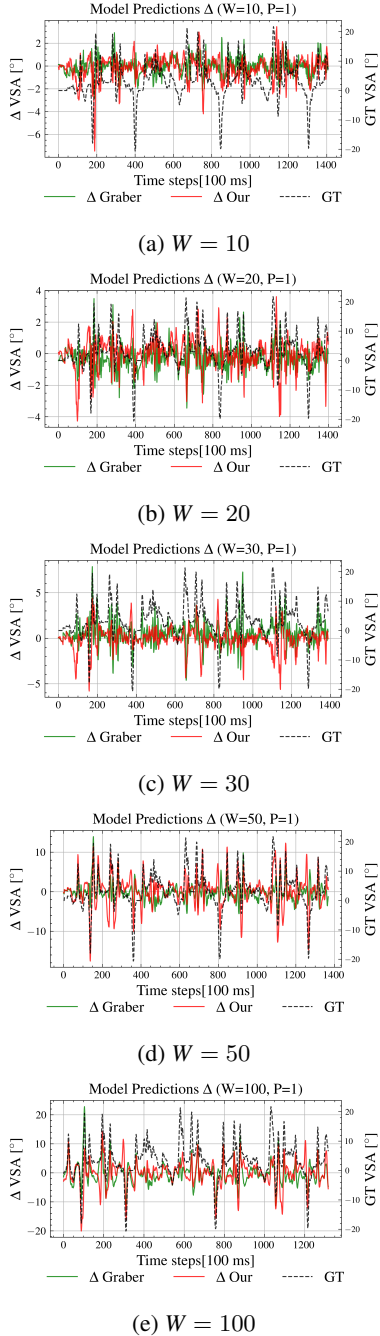


Fig. 10. S2O differential plots of **Approach A** for window sizes $W = \{10, 20, 30, 50, 100\}$ and prediction horizons $P = 1$

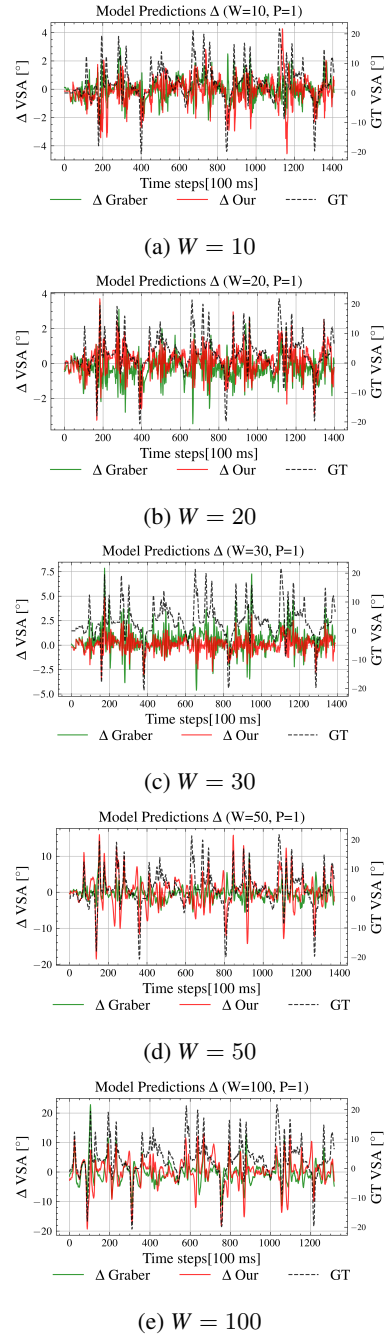


Fig. 11. S2O differential plots of **Approach B** for window sizes $W = \{10, 20, 30, 50, 100\}$ and prediction horizons $P = 1$

Appendix B. S2S Average Error Comparison

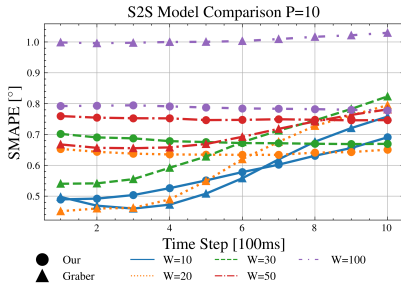
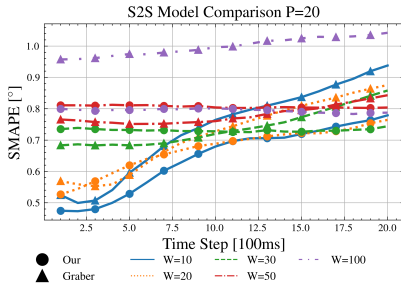
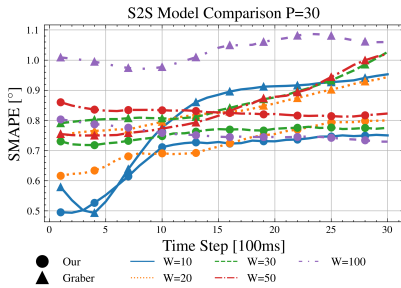
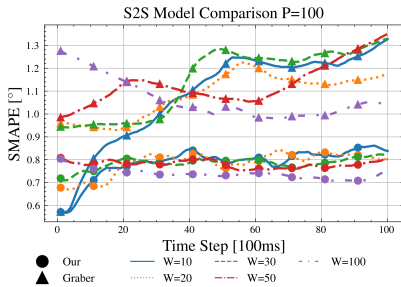
(a) $P = 10$ (b) $P = 20$ (c) $P = 30$ (d) $P = 100$

Fig. 12. S2S averaged sMAPE comparison for **Approach A** for different horizons P

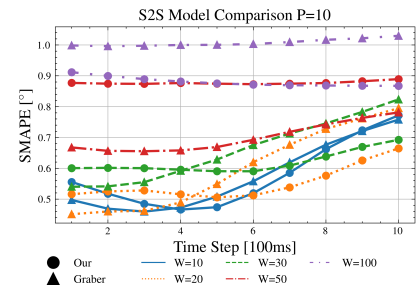
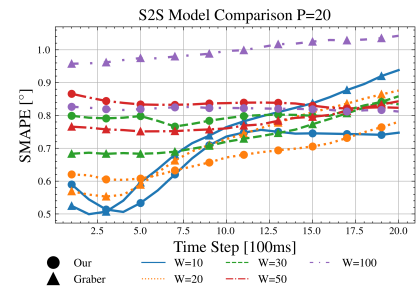
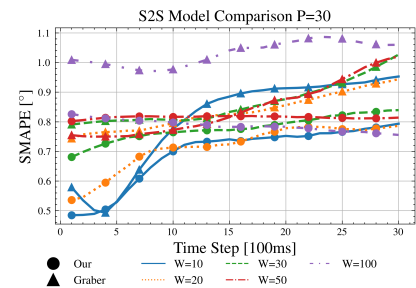
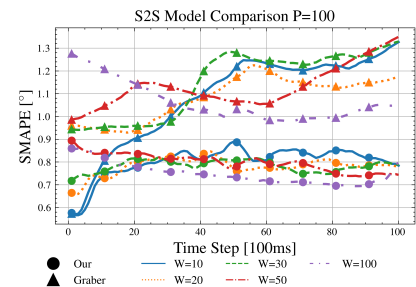
(a) $P = 10$ (b) $P = 20$ (c) $P = 30$ (d) $P = 100$

Fig. 13. S2S averaged sMAPE comparison for **Approach B** for different horizons P